Joint inversion of seismic and electric data applied to 2D media

GEOPHYSICS, VOL. 80, NO. 4 (JULY-AUGUST 2015); P. EN93–EN104, 11 FIGS., 3 TABLES.
10.1190/GEO2014-0313.1

Joint inversion of seismic and electric data applied to 2D media

Flora Garofalo[1], Guillaume Sauvin[2], Laura Valentina Socco[1], and Isabelle Lecomte[3]

ABSTRACT

Methods based on the seismic P-wave, seismic surface wave, and apparent resistivity are commonly used in the solution of several near-surface problems. However, the solution nonuniqueness and the intrinsic limitations of these methods can cause inconsistency in the final results. Dispersion curves of surface waves, P-wave traveltimes, and apparent-resistivity data were jointly inverted to obtain internally consistent and more reliable final model of P- and S-wave velocities and resistivity. A collection of 1D layered models was obtained by a deterministic joint-inversion algorithm based on the laterally constrained inversion scheme. The three data sets were jointly inverted imposing the same structure and Poisson's ratio was introduced as a physical link between P- and S-wave velocities to better constrain the inversion. No physical link was imposed between the resistivity and the seismic velocities. The inversion algorithm was tested on synthetic data and then applied to a field case, where benchmark borehole data were available. The synthetic and field examples provided results in agreement with the true model and the existing geologic information, respectively.

INTRODUCTION

In near-surface geophysics, electric and seismic methods are widely used in various applications. They are based on different physical phenomena, and hence they investigate different properties of the subsurface. Among the seismic techniques, surface-wave analysis (SWA) is commonly used to estimate the S-wave velocity, whereas body-wave tomography (BWT) is applied to retrieve the P-wave velocity distribution. These results are useful for various engineering and environmental applications, e.g., for seismic hazards, geotechnical characterization, and hydrogeophysical characterization. Electric methods, such as continuous vertical electric sounding (CVES) or electrical resistivity tomography (ERT), are used to map the electric resistivity. They have several near-surface applications such as detection of groundwater resources; monitoring of polluted sites; landfill mapping; or the location of cavities, faults, and permafrost.

Seismic and electric methods are based on the solution of inverse problems, which are affected by solution nonuniqueness, ill posedness, and/or lack of resolution. The final model is then subject to interpretation ambiguities.

In SWA, the inversion problem is ill posed, strongly nonlinear, mixed-determined, and it is affected by solution nonuniqueness (Luke et al., 2003). Different strategies have been proposed to mitigate these problems; some authors (Press, 1968; Beaty et al., 2002; Feng et al., 2005; Dal Moro et al., 2007) propose to use stochastic approaches to optimally sample the model-parameter space, whereas others (Lai, 1998; Xia et al., 1999; Socco et al., 2009) suggest the use of constraints and a priori information to improve the solution reliability of deterministic methods.

BWT is solved as an inverse problem in which a 2D P-wave velocity mesh-grid model is inferred from P-wave traveltimes. To do so, different strategies have been devised, e.g., deterministic algorithms, including singular value decomposition (Meyer, 2000) and the simultaneous iterative technique (Lo and Inderwiesen, 1994), or probabilistic ones, such as genetic algorithms (Michalewicz, 2000). The main limitation of these methods arises when a subsurface layer cannot be detected, i.e., the "hidden-layer" problem. This is mostly due to a strong velocity contrast, a layer too thin to be detected, a velocity inversion, or inadequate receiver spacing (Soske, 1959).

The CVES method derives a resistivity model from the inversion of the apparent resistivity, and it can be affected by interpretation ambiguities, such as equivalence and/or suppression problems. The first occurs when different vertical resistivity profiles lead to the same value of apparent resistivity, and hence no differences are de-

Manuscript received by the Editor 10 July 2014; revised manuscript received 17 December 2014; published online 29 May 2015.
[1]Politecnico di Torino, Turin, Italy. E-mail: flora.garofalo@polito.it; valentina.socco@polito.it.
[2]Formerly University of Oslo, Department of Geosciences International Centre for Geohazards and NORSAR, Oslo, Norway; presently Norwegian Geotechnical Institute, Oslo, Norway. E-mail: gillaume.sauvin@ngi.no.
[3]University of Oslo, Department of Geosciences International Centre for Geohazards and NORSAR, Oslo, Norway. E-mail: isabelle.lecomte@norsar.no.

tected in the experimental data. The latter happens when an intermediate layer is characterized by a resistivity value contrasting with the adjacent ones, within an increasing or decreasing resistivity profile with depth, and the experimental data may not be sensitive to that layer.

To mitigate issues encountered for each inverse problem, joint inversion of different kinds of data can be applied. The sensitivity to model parameters of each method can be exploited and hence in many cases joint inversion allows the inherent limitations of each technique to be reduced. One of the first examples of the joint-inversion algorithm is proposed by Vozoff and Jupp (1975) for magnetotelluric and resistivity data. Following this publication, several authors propose similar algorithms combining different data sets and imposing the same geometry to the model (e.g., Linde et al., 2006; Hu et al., 2009; Jegen et al., 2009; Doetsch et al., 2010; Moorkamp et al., 2011) or using some petrophysical relationships among the model parameters (e.g., Gao et al., 2010, 2011; Dell'Aversana et al., 2011). Some authors such as Hering et al. (1995) and Misiek et al. (1997) combine surface-wave dispersion and apparent-resistivity data, whereas others (Gallardo and Meju, 2003, 2004; de Nardis et al., 2005) focus on the joint inversion of apparent-resistivity and P-wave refraction data. Previous studies (Comina et al., 2002; Piatti et al., 2013) show that joint inversion also performs better than individual inversion in those cases, in which one of the geophysical parameters presents variations that the other parameters do not. In particular, Comina et al. (2002) propose a 1D joint inversion of surface-wave and apparent-resistivity data and test it on a synthetic model in which the resistivity does not vary, while the S-wave velocity does vary. Piatti et al. (2013) propose a 1D joint inversion between surface-wave data and P-wave traveltimes and successfully apply it to a field case in which the P-wave velocity almost does not vary while the S-wave velocity presents a very sharp variation. They also show that low S- and P-velocity layers embedded within stiffer layers that cannot be retrieved by individual inversions can be resolved by applying joint inversion (see the supplementary material for a further example; it can be accessed at s1.pdf).

Here, we present an algorithm for the joint inversion of dispersion curves of the surface wave, P-wave refraction traveltimes, and apparent-resistivity data using a structural approach and physical links. These three methods are already used in a joint structural inversion by Kis et al. (1995), who propose a least-squares joint-inversion algorithm for geoelectric, seismic surface-wave, and P-wave refraction data. The algorithm proposed here differs from Kis et al. (1995) with the additional use of the Poisson's ratio as a physical link between the P- and S-wave velocities and with the spatial regularization introduced among 1D seismic and resistivity models. The use of Poisson's ratio as physical constraint between seismic velocities allows derivation of an internally consistent velocity model, as shown by Dal Moro (2008), Piatti et al. (2013), and Boiero and Socco (2014). The proposed algorithm is based on the one defined for 2D layered models by Boiero and Socco (2014), but, in addition to surface-wave dispersion and P-wave refraction data, we extend the method to include apparent-resistivity data.

After the description of the algorithm, we show the benefit of the joint inversion with respect to the individual ones on a synthetic case study. We use on purpose a very simple model, in which all the parameters vary at the interfaces. After the test on the synthetic model, we present the application of the algorithm on a real case study.

METHOD

The subsurface is investigated along a line using SWA, BWT, and CVES, and the associated experimental data are surface-wave dispersion curves, P-wave traveltimes, and apparent-resistivity curves, respectively. These data are inverted all together using a least-squares inversion algorithm, and the final model is solved not only by imposing the same structure but also by applying a physical link among the model parameters. The algorithm presented here is based on the one proposed by Boiero and Socco (2014), and it is supplemented with resistivity. Hence, we use the same notation and we only describe in detail the implementation of the resistivity in the algorithm proposed by Boiero and Socco (2014). We refer the reader to that publication for further details on the method.

Data and model parameterization

Surface-wave dispersion curves $\mathbf{dc}\ (x, f)$ (phase velocity as a function of frequency f) are locally extracted in the x positions by applying a moving spatial window along the seismic line (Socco et al., 2009), and they are obtained as energy maxima in the frequency-wavenumber domain. For every window position, several shots are processed allowing the experimental uncertainties on phase velocity $\mathbf{e_{obs,dc}}(x, f)$ to be estimated.

P-wave first-break traveltimes $\mathbf{fb}(x, sp)$ are a function of x and the source position sp, and they are picked on the seismogram at each receiver along the line. Experimental uncertainties $\mathbf{e_{obs,ar}}(x, es)$ can be estimated as a fixed value related to the time-sampling interval or as a standard deviation if the picking procedure is repeated several times.

The apparent-resistivity curves $\mathbf{ar}(x, es)$ are estimated at positions x as a function of the electrode spacing es, and $\mathbf{e_{obs,ar}}(x, es)$ is the vector of the associated uncertainties. Apparent-resistivity values are extracted from the apparent-resistivity pseudosection within a bin, usually two times the electrode spacing, centered on the locations where dispersion curves are available.

Once all the data are collected, they are gathered in the experimental data vector $\mathbf{d_{obs}}$ as follows:

$$\mathbf{d_{obs}} = [\mathbf{dc}(x, f);\ \mathbf{fb}(x, sp);\ \mathbf{ar}(x, es)], \tag{1}$$

and the associated covariance matrix $\mathbf{C_{obs}}$ is defined as

$$\mathbf{C_{obs}} = \mathrm{cov}[\mathbf{e_{obs,dc}}(x, f);\ \mathbf{e_{obs,fb}}(x, sp);\ \mathbf{e_{obs,ar}}(x, es)]. \tag{2}$$

Such a matrix is diagonal because the experimental uncertainties are supposed to be uncorrelated.

The model parameterization is based on a pseudo-2D model: the model vector $\mathbf{m}$ is a collection of K 1D-layered models, located at the positions x. Each 1D kth model $\mathbf{m_k}$ is made up by n_l layers over a half-space, and each ith layer is defined in terms of thickness h_i (except for the half-space), density (ρ_i), S-wave velocity ($V_{S,i}$), P-wave velocity ($V_{P,i}$), and resistivity (Rho_i). Because the involved methods have very low sensitivity to the density (Xia et al., 1999), the values of this parameter are assumed a priori. Hence, the vector of unknown model parameters at the kth position is given by

$$\mathbf{m_k} = [h_1 \cdots h_{nl}\ V_{S,1} \cdots V_{S,nl+1}\ V_{P,1} \cdots V_{P,nl+1}\ Rho_1 \cdots Rho_{nl+1}]^T. \tag{3}$$

Thus, the model vector $\mathbf{m}$ is given by

$$\mathbf{m} = [\mathbf{m}_1; \ldots; \mathbf{m}_K]. \tag{4}$$

Because we solve the inverse problem with a local-search algorithm, an accurate choice of the initial model is needed to avoid falling into a local minimum. Moreover, we use a layered model and the number of layers must be carefully chosen to account for each model-parameter variability. In fact, there could be variations for one parameter (i.e., resistivity) that do not correspond to variation for the others (i.e., seismic velocities), and vice-versa. The number of layers must therefore be selected to allow for the required variability but also to avoid overparameterization that would lead to poor sensitivity. The initial model can be defined on the basis of a priori information or deduced from the data. In absence of a priori information, the initial model of V_S and V_P can be defined as suggested by Piatti et al. (2013), who propose a 1D joint inversion of surface-wave dispersion and P-wave traveltime data. Similarly to Piatti et al. (2013), we first define a V_P model, using the intercept-time method on one representative hodochrone along the line. The corresponding V_S model is then built by assuming the Poisson's ratio values expected for the considered materials. The *Rho* model is defined as the apparent resistivity at the pseudodepths corresponding to the interfaces of the V_P model. Therefore, the number of layers is defined on the basis of P-wave information, but this value is usually increased to cope with possible variations of other parameters that are not detected on the V_P profile. Typically, it will be necessary to increase the number of layers when a water table is expected within the reached investigation depth because V_P will tend to exhibit poor variability in the saturated material, whereas V_S will better depict the variability of the solid matrix properties.

The algorithm

The least-squares joint-inversion algorithm is based on structural coupling, where the layer boundaries are solved minimizing the misfit between the theoretical and all the experimental data, and a physical link $pr(\mathbf{m})$ among the model parameters is introduced. As proposed by Boiero and Socco (2014), the seismic velocities V_S and V_P are linked to each other by imposing constraints on the Poisson's ratio values. This constraint represents a priori information that can be included in the joint-inversion process. Other a priori information can be introduced in the form of regularization. In particular, because we deal with a collection of spatially distributed 1D models, a spatial regularization is applied. The adopted scheme is the one proposed by Auken and Christiansen (2004) for the inversion of resistivity data, and then applied by Socco et al. (2009) to surface-wave dispersion data, and used by Boiero and Socco (2014) for surface-wave and P-wave refraction data. The spatial regularization constrains the variation of each model parameter between neighboring models. In addition, the model parameters can also be constrained to their value in the initial model. The availability of a priori information can significantly improve the inversion results, but it can also bias the results, and hence, its effects must be weighted according to the information reliability (uncertainty).

The final model $\mathbf{m}$ is solved through the minimization of the following misfit function Q, as proposed by Boiero and Socco (2014):

$$\begin{aligned} Q = &[(\mathbf{d_{obs}} - fw(\mathbf{m}))^T \mathbf{C_{obs}^{-1}} (\mathbf{d_{obs}} - fw(\mathbf{m}))] \\ &+ [(\mathbf{m_{prior}} - \mathbf{m})^T \mathbf{C_{prior}^{-1}} (\mathbf{m_{prior}} - \mathbf{m})] \\ &+ [(-\mathbf{Rm})^T \mathbf{C_R^{-1}} (-\mathbf{Rm})] \\ &+ [(\mathbf{pr} - pr(\mathbf{m}))^T \mathbf{C_\nu^{-1}} (\mathbf{pr} - pr(\mathbf{m}))], \end{aligned} \tag{5}$$

where $\mathbf{m_{prior}}$ is the initial model, and $\mathbf{C_{prior}}$ is its covariance matrix. The spatial regularization consists of the matrix $\mathbf{R}$, as explained in Auken and Christiansen (2004), where the strength of the link is expressed by the covariance matrix $\mathbf{C_R}$. The physical link implies the minimization of Poisson's ratio of the model $pr(\mathbf{m})$ with respect to an expected value $\mathbf{pr}$, and the weight of this information is expressed by the covariance matrix $\mathbf{C_\nu}$.

The addition of the apparent-resistivity data affects not only the $\mathbf{d_{obs}}$ and the $\mathbf{m}$ vectors, but also the forward response $fw(\mathbf{m})$ that accounts for the contributions of the three methods:

$$fw(\mathbf{m}) = \begin{bmatrix} fw_{\mathrm{SWA}}(\mathbf{m}) \\ fw_{\mathrm{BWT}}(\mathbf{m}) \\ fw_{\mathrm{CVES}}(\mathbf{m}) \end{bmatrix}, \tag{6}$$

where $fw_{\mathrm{SWA}}(\mathbf{m})$, $fw_{\mathrm{BWT}}(\mathbf{m})$, $fw_{\mathrm{CVES}}(\mathbf{m})$, are the forward responses used for SWA, BWT, and CVES, respectively. The formulation for $fw_{\mathrm{SWA}}(\mathbf{m})$ is based on the Haskell-Thomson model (Thomson, 1950; Haskell, 1953), and the Cole-Cole model (Cole and Cole, 1941) is adopted for $fw_{\mathrm{CVES}}(\mathbf{m})$. The $fw_{\mathrm{SWA}}(\mathbf{m})$ and $fw_{\mathrm{CVES}}(\mathbf{m})$ are based on 1D formulations and are computed for each 1D model. Conversely, $fw_{\mathrm{BWT}}(\mathbf{m})$ is computed according to the 2D formulation proposed by Podvin and Lecomte (1991), in which the 2D mesh-grid model is obtained from linear interpolation of the 1D models.

Equation 5 is minimized using a quasi-Newton damped least-squares algorithm (Tarantola, 1987; Aster et al., 2005). At each iteration n, the problem defined in equation 5 is linearized around model $\mathbf{m_n}$ and the misfit is minimized following the local decrease of the misfit function itself. Hence, at the nth iteration, the model $\mathbf{m_n}$ is updated in $\mathbf{m_{n+1}}$ as follows:

$$\begin{aligned} \mathbf{m_{n+1}} = &\mathbf{m_n} \\ &+ \left(\begin{array}{l} [\mathbf{G_J^T C_{obs}^{-1} G_J} + \mathbf{P^T C_{prior}^{-1} P} + \mathbf{R^T C_R^{-1} R} + \mathbf{G_{pr}^T C_{pr}^{-1} G_{pr}} + \lambda \mathbf{I}]^{-1} \\ \quad \times \begin{bmatrix} \mathbf{G_J^T C_{obs}^{-1}} (\mathbf{d_{obs}} - fw(\mathbf{m_n})) + \mathbf{P^T C_{prior}^{-1}} (\mathbf{m_{prior}} - \mathbf{m_n}) \\ + \mathbf{R^T C_R^{-1}} (-\mathbf{R m_n}) + \mathbf{G_{pr}^T C_{pr}^{-1}} (\mathbf{pr} - pr(\mathbf{m})) \end{bmatrix} \end{array} \right), \end{aligned} \tag{7}$$

where λ is a damping factor that is updated at each iteration; it stabilizes the solution and ensures convergence as proposed by Levenberg (1944) and Marquardt (1963).

The iterative process stops when one of the following criteria is matched: (1) a defined number of iterations is reached (in our case 60) or (2) the value of misfit Q related to the update model $\mathbf{m_{n+1}}$ reduces less than 1% with respect to the value at the previous iteration n.

Matrix $\mathbf{P}$ represents the partial derivatives of $\mathbf{m_{prior}}$ with respect to the unknowns. The matrix $\mathbf{G_{pr}}$ contains the partial derivatives of the physical link with respect to the unknowns. The matrix $\mathbf{G_J}$ is the Jacobian, representing the sensitivity matrix of the data, and it is

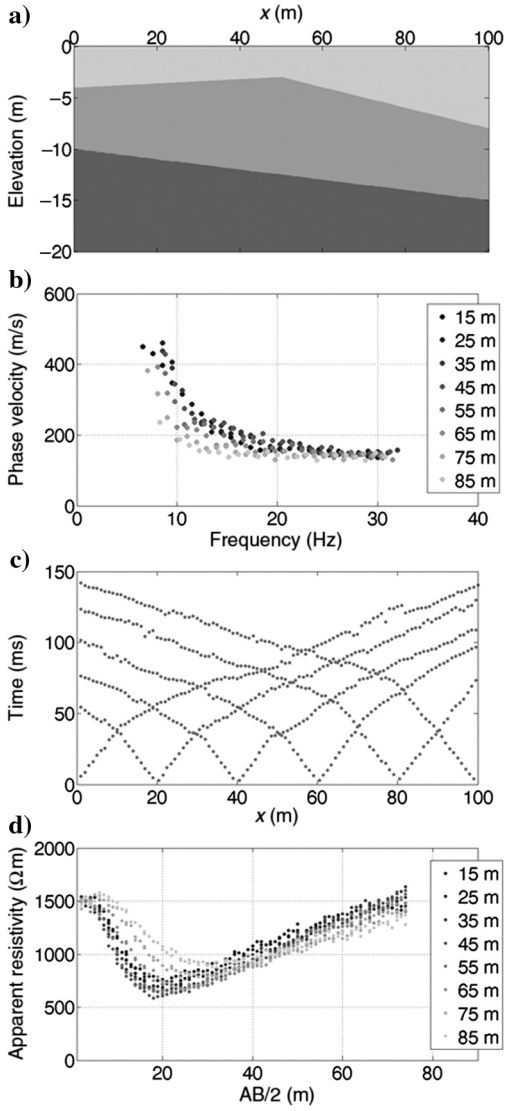

Figure 1. (a) Synthetic model made up of three layers. The properties of each layer are reported in Table 1. (b) Surface-wave dispersion curves in which the gray scale corresponds to the positions along the line. (c) P-wave traveltimes. (d) Apparent-resistivity curves extracted at the same positions of the surface-wave dispersion curves. The gray scale corresponds to the positions along the line.

built up with the sensitivity relevant to each type of data $\mathbf{G}_{\mathbf{J,SWA}}$, $\mathbf{G}_{\mathbf{J,BWT}}$, and $\mathbf{G}_{\mathbf{J,CVES}}$:

$$\mathbf{G_J} = \begin{bmatrix} \mathbf{G}_{\mathbf{J,SWA}} \\ \mathbf{G}_{\mathbf{J,BWT}} \\ \mathbf{G}_{\mathbf{J,CVES}} \end{bmatrix}. \tag{8}$$

Because we deal with different kinds of model parameters, Boiero and Socco (2014) suggest a normalization strategy based on Hering et al. (1995), which consists in the normalization of $\mathbf{m}$ and all the quantities related to it with respect to $\mathbf{m_n}$ (for details, see Boiero and Socco, 2014).

SYNTHETIC DATA

In this section, we show the application of the joint inversion algorithm to synthetic data, which is aimed at showing the improvement of the joint inversion with respect to the individual inversions. The synthetic model was kept very simple, and the model parameterization for inversion was the same as the true model. This example may not seem challenging, but we will show that, even in these favorable conditions, individual inversions may fail in estimating the model parameter values, which are instead retrieved by joint inversion. Moreover, two additional synthetic examples are provided in the supplementary material, which can be accessed online at s1.pdf.

Synthetic model and data

We define a 2D model characterized by two layers over a half-space (Figure 1a) with a laterally varying geometry so that the thickness, which represents the coupling element among different models, is smoothly horizontally varying. The physical parameters are constant within each layer (Table 1), with the seismic velocities V_S and V_P increasing with depth, and the resistivity *Rho* is lower in the intermediate layer than in the others.

The seismic data set was obtained by a finite-element simulation performed with COMSOL Multiphysics® software. The source was a Ricker wavelet, and the shot and receiver spacing were equal to 20 and 1 m, respectively, along a 100-m line. We extracted the surface-wave dispersion curves applying a 30-m spatial moving window, where neighboring windows have 66% overlap. The eight resulting dispersion curves are shown in Figure 1b, whereas the manually picked P-wave traveltimes are reported in Figure 1c. The seismic data were affected by numerical noise (see Figure 1b and 1c).

Table 1. Properties of the synthetic model: Thickness *h*, density ρ, Poisson's ratio ν, S-wave velocity V_S, P-wave velocity V_P, and resistivity *Rho*. The true and initial models are provided.

	Layer	*h* (m)	ρ (kg/m^3)	ν (–)	V_S (m/s)	V_P (m/s)	*Rho* (Ωm)
True model	1	3–8	1800	0.288	150	275	1500
	2	6–9.5	1850	0.408	275	700	500
	Half-space	—	1900	0.367	550	1200	3000
Initial model	1	6.5	1800	0.33	100	200	1500
	2	4.5	1850	0.33	375	750	800
	Half-space	—	1900	0.33	500	1000	1500

The apparent resistivity was estimated using RES2DMOD software (Loke, 2002). To get enough penetration depth and resolution, we defined an array of 200 electrodes with 1-m spacing centered on our model and we simulated a dipole-dipole configuration. A 2.5% noise was added to the data, and the apparent-resistivity curves were extracted at the same positions as for the dispersion curves. The apparent-resistivity curves are shown in Figure 1d. We associated an uncertainty equal to 5% to all the data.

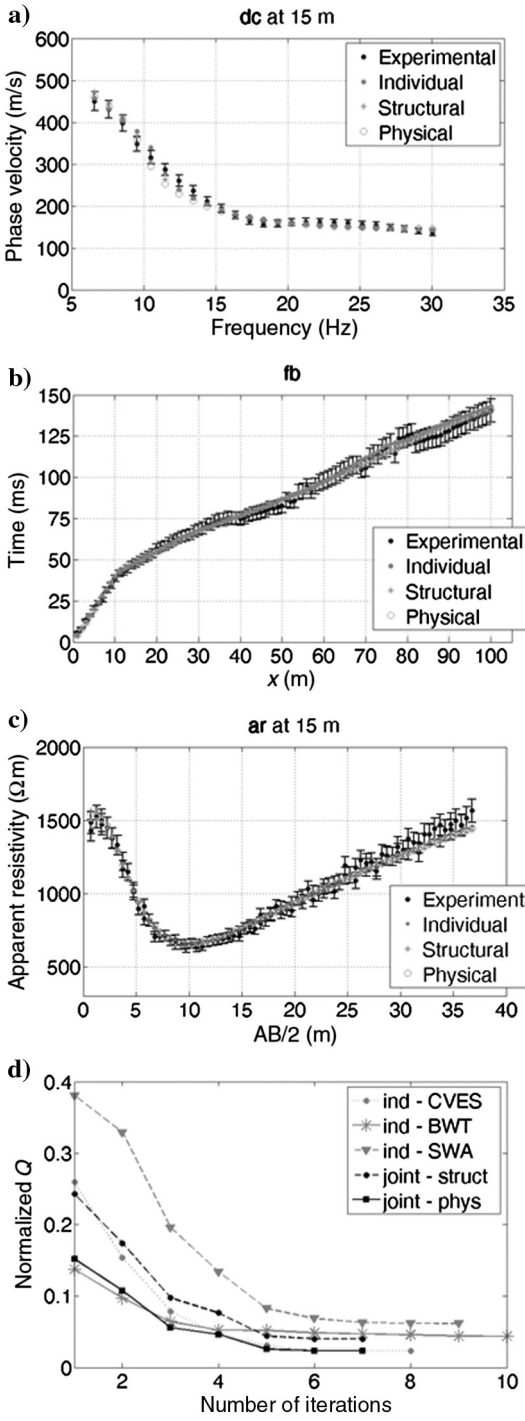

Figure 2. An example of the comparison among the data and the forward responses of the final models obtained through different inversions: individual, structural, and physical. (a) The dispersion curve at $x = 15$ m, (b) apparent-resistivity curve at position $x = 15$ m, (c) P-wave traveltimes for the shot at $x = 0$ m, and (d) comparison of misfit value Q (normalized for the number of data points) at each iteration. This is evaluated for the different inversions.

Initial model and inversion results

The initial model was laterally homogeneous to verify if the laterally varying geometry can be well reconstructed. First, we estimated a 1D V_P model through the intercept-time method applied on P-wave traveltimes shot at $x = 100$ m. We derived S-wave velocity V_S from V_P, after assuming a Poisson's ratio of 0.33. We estimated resistivity *Rho* from the apparent-resistivity data at the pseudodepths corresponding to the interfaces estimated from the intercept-time method. The retrieved 1D model (Table 1) was used as the initial model for the inversion without introducing lateral variations along the line.

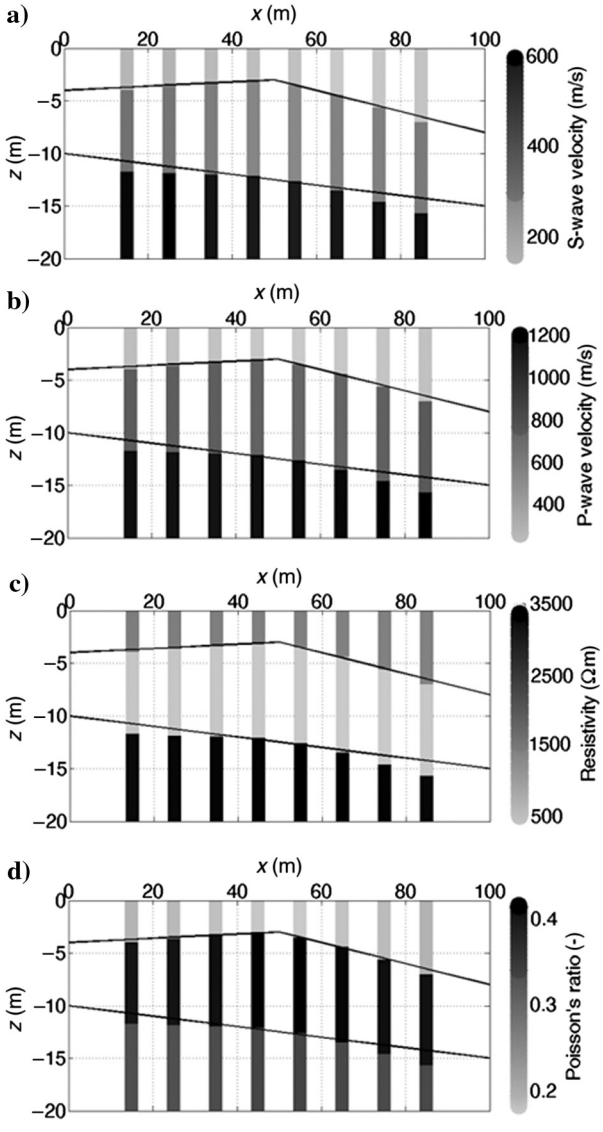

Figure 3. Results of the physical joint inversion for the synthetic model: (a) S-wave velocity model, (b) P-wave velocity model, (c) resistivity model, and (d) Poisson's ratio model. The black continuous lines are the interfaces of the true model.

As far as the a priori information setting is concerned, the $\mathbf{m}_{\mathbf{prior}}$ was equal to the initial model, whereas the expected values **pr** of the Poisson's ratio were equal to 0.33 for all the layers. The constraints of the whole a priori information were set very weak to focus the solution on the contribution of the experimental data only. Therefore, the diagonal elements of the covariance matrices $\mathbf{C}_{\mathbf{R}}$, $\mathbf{C}_{\mathbf{prior}}$, and $\mathbf{C}_{\boldsymbol{\nu}}$ in equation 5, were set equal to 10^6 as suggested by Boiero and Socco (2010) to have almost no influence of these pieces of a priori information on the final model.

Several inversions were performed with the same initial model and constraints on the a priori information: (1) "individual" inversion, where each data set was inverted separately, (2) "structural" inversion, where all the data were jointly inverted using only the layer thickness as coupling factor, and (3) "physical" inversion, where the physical link between V_P and V_S was applied in addition to the structural inversion.

The final models from different inversions provided very good fitting with the data (Figure 2a–2c). Figure 2d shows how the misfit Q, normalized for the number of data points, varies at each iteration for all the inversions performed. The physical joint inversion stopped before the individual inversions (7 iterations against 10 of the individual BWT), and it has a lower misfit Q than the structural joint inversion.

Here, we only present the final pseudo-2D model obtained through the physical joint inversion (Figure 3), in which the interface depths match quite well with the true ones. Although the expected value of the Poisson's ratio **pr** was set equal to 0.33 for all layers, the distribution of this parameter (Figure 3d) was well retrieved.

We show in Figure 4 the error between the true model and the final ones obtained through the different kind of inversions for the 1D model at 55 m. The trends are similar for all the other 1D models. In the individual inversions, some model parameters were better resolved whereas others, such as the layer thicknesses, were less-well resolved. The joint inversions slightly increased the error of such well-estimated parameters as V_P and V_S in the second layer, from 4.5% to 8% and from 2% to 4.5%, respectively, but they significantly reduced all the other errors. As far as the layer thickness is concerned, SWA provided a good estimation with an error lower than 5%, whereas for BWT and CVES, the error was greater than 10% reaching almost 30%. The structural inversion improved the estimation of the thicknesses, reducing the error to less than 5%, and this error was further reduced when the physical link was applied. In addition, all of the other model parameter errors decreased below 10% with the joint inversions, except for the resistivity of the half-space.

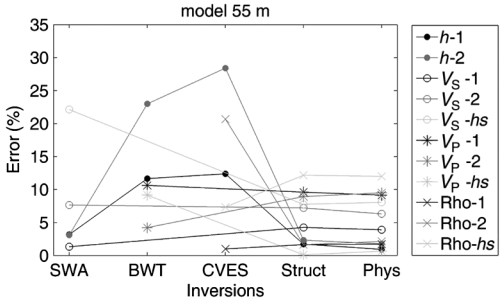

Figure 4. Synthetic model: Errors between the final model from the different inversions and the true one calculated at position 55 m. The error is computed for each model parameter: thickness h, S-wave velocity V_S, P-wave velocity V_P, and resistivity *Rho* for layers 1, 2, and the half-space (1, 2, and *hs*, respectively, in the legend). The different inversions are as follows: only SWA, only BWT, only CVES, all the data together (Struct), and with the addition of the physical link (Phys).

FIELD EXAMPLE

Site description and experimental data

The field data were acquired in a landslide-prone area close to the city of Hvittingfoss, located 80 km southwest of Oslo, Norway (Figure 5). This site was investigated using geophysical methods as part of a stability assessment project aimed at detecting the highly sensitive clay responsible for instability. The geologic model consists of a thin

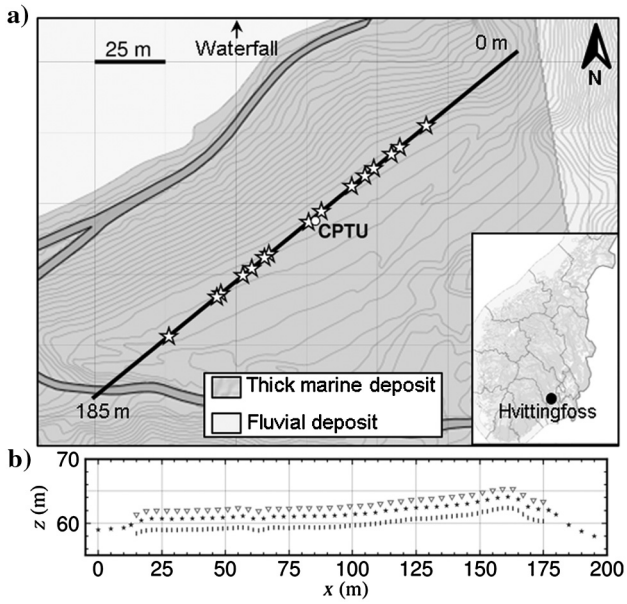

Figure 5. The Hvittingfoss field case: (a) Quaternary map with 5-m contour line topography superimposed; the black line locates the profile in which the white stars indicate the 1D model positions and the circle indicates the position of the CPTU well. (b) Detailed shot (stars), geophone (reversed triangles), and electrode (vertical dashes) locations and elevations along the profile are displayed.

Table 2. Hvittingfoss field case. Acquisition parameters of the experimental data.

Methods	Parameters	
ERT	Acquisition system	Terrameter LS
	Array type	Dipole-dipole
	Electrode spacing	2 m
	Profile length	185 m
BWT	Acquisition system	Geode seismograph
	Source	Sledgehammer 5 kg
	Recording length	2 s
	Sampling	0.25 ms
	Receiver spacing	4 m
	Source spacing	4 m
	Profile length	185 m

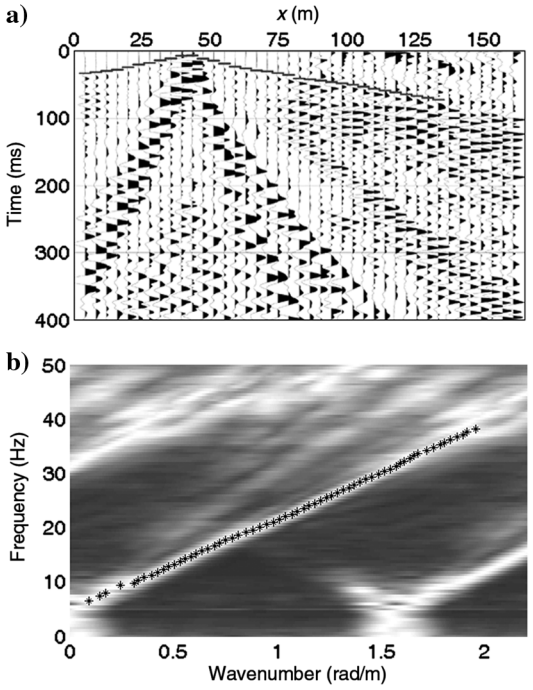

Figure 6. The Hvittingfoss field case: (a) Example of the P-wave shot gather at 117 m. For the sake of display, a 250-ms automatic gain control is applied. The first-arrival traveltime picks are also shown (gray dashes). (b) Normalized f-k spectrum, for a window centered at 53 m, in which the black asterisks represent the picked dispersion curve.

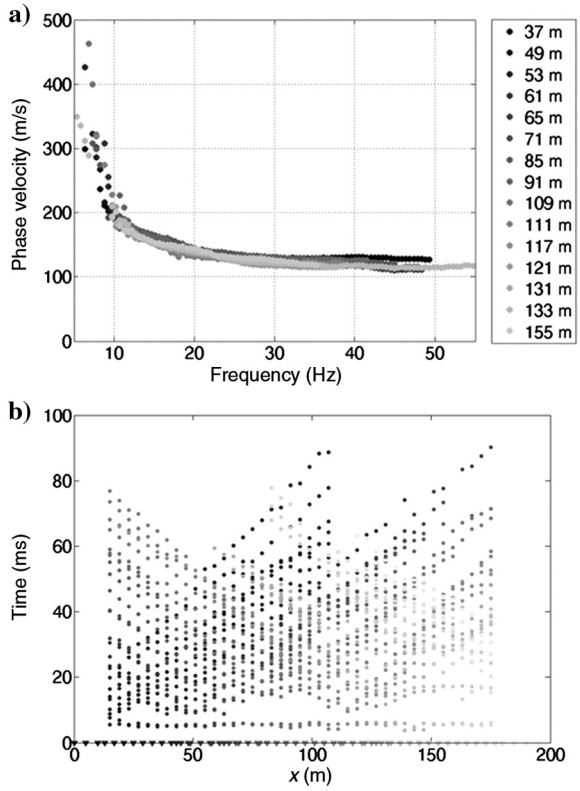

Figure 7. The Hvittingfoss field case: (a) Surface-wave dispersion curves; the grayscale corresponds to the location along the line. (b) P-wave traveltimes (dots); the grayscale corresponds to the shot locations (triangle) along the line.

fluviodeltaic layer, mainly composed of sand and gravel, overlaying a thick marine-clay deposit. Previous results from geotechnical investigations and geophysical data analyses (Sauvin et al., 2013) were used as a benchmark for our joint inversion result. In particular, S-wave seismic reflection sections provided stratigraphy for the marine deposit. The V_S field was evaluated during the velocity analysis performed for S-wave seismic reflection processing and was compared with the joint inversion result. Other comparisons were performed with BWT and ERT that provided smooth V_P and *Rho* models. Geotechnical soundings, as well as resistivity- and seismic-cone penetration tests (R-CPTU and S-CPTU, respectively) were also available. Several ground-penetrating-radar (GPR) profiles were performed in the area.

Seismic and electric data were available along a 185-m profile, and the acquisition parameters are summarized in Table 2. The picking of P-wave traveltimes was performed manually on raw data because the presence of noise did not allow for automatic picking. We show an example of a P-wave seismic shot gather with the picked traveltimes in Figure 6a and an example of the normalized f-k spectrum with the picked dispersion curve in Figure 6b. Figure 7a presents the P-wave traveltime data for the whole data set. We extracted 15 surface-wave dispersion curves (Figure 7b) along the line using different spatial windows varying between 12 and 20 channels with an overlap of approximately 70%. The retrieved frequency band ranges from 8 to 40 Hz with the wavelength varying from approximately 40 to 3 m. For the resistivity, we use a dipole-dipole configuration with a classical ERT acquisition. From these data, 15 CVES apparent-resistivity curves were extracted at the same positions at which the dispersion curves were estimated. Figure 8 shows the pseudosection and the positions at which the apparent-resistivity curves were extracted.

As far as the data quality is concerned, no data were discarded from the apparent-resistivity data set and data uncertainties were directly derived from the variance of each measurement provided by the measurement equipment and have an average of 16.2%. Regarding seismic data, the 22% of the traces were not picked due to the poor signal-to-noise ratio and a 5% uncertainty was assigned to the P-wave traveltime values and to the surface-wave dispersion curves.

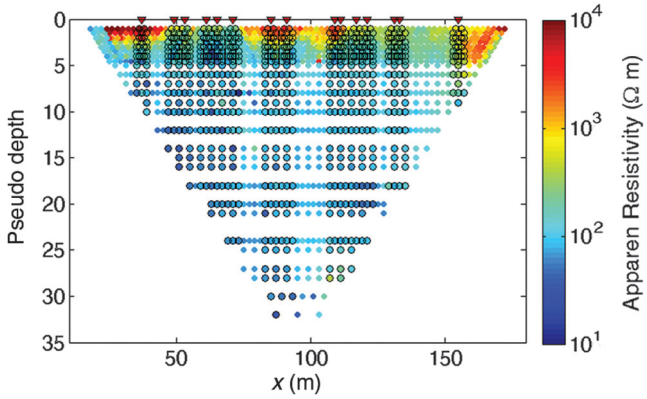

Figure 8. The Hvittingfoss field case: Logarithm of apparent resistivity as a function of the pseudodepth. The triangles correspond to the positions at which the 1D apparent-resistivity curves (circles) were extracted.

Model parameterization and inversion results

The initial model was defined on the basis of general knowledge about the geology of the site. In particular, we assigned a layer to the thin sand unit on the top and three layers (two layers plus the half-space) to the underlying clay unit (the model parameters are given in Table 3). The initial model did not present lateral variations, and the values of the model parameters were defined on the basis of preliminary analyses of data (Figures 7 and 8). We set weak spatial regularization by setting the diagonal elements of matrix $\mathbf{C_R}$ (equation 5) equal to 10^4 as suggested by Boiero and Socco (2010). No constraints with respect to the initial model, including Poisson's ratio values, were set.

The physical joint inversion converged rapidly (within 13 iterations; see Figure 9a) with a good fitting between the experimental data and forward response. A representative example of fitting is reported in Figure 9b–9d for the surface-wave dispersion curve, P-wave traveltimes, and apparent-resistivity curve, respectively. For almost the whole data set, the misfit is below the experimental uncertainty. We present the physical joint inversion result in Figure 10 superimposed to V_P, V_S, and *Rho* models derived from previous P-wave refraction tomography, S-wave reflection seismic velocity analysis, and ERT, respectively. The results of the R-CPTU and S-CPTU are also reported over the *Rho* and V_S models, respectively. We also present the comparison between the Poisson's ratio resulting from the physical joint inversion with the one computed from the V_P and V_S estimated in the previous studies.

We compared the final model of the joint inversion with the previous results at the locations, where the 1D models were estimated. In the sand deposit, the differences between the model parameter values obtained by joint inversion and previous results range from 6.7% to 12.3% for V_S, 8.4% to 22.1% for V_P, and 18.7% to 21.9% for *Rho*. In the clay deposit, the differences vary from 7.4% to 11.9% for V_S, 10.5% to 19.3% for V_P, and 9.8% to 23.1% for *Rho*.

The smooth lateral variation is well recovered despite the adopted 1D forward model for surface waves and resistivity in the joint inversion. The layered model assisted the interpretation, and thicknesses derived from joint inversion better correlated with the geotechnical data and S-wave seismic reflection section. Moreover, the thickness of the shallow sand layer that overlies the clay deposit retrieved by the GPR profiles is in very good agreement with the joint inversion result. Because none of GPR profiles is coincident with our profile, we compared the depth of the sand/clay boundary, interpolated from the GPR profiles (the white line in Figure 10b) at our location with the one derived from joint inversion. The average depth difference is 0.65 m.

Table 3. Hvittingfoss field case: initial model adopted for the physical joint inversion.

Layer	h (m)	ρ (kg/m^3)	ν (–)	V_S (m/s)	V_P (m/s)	*Rho* (Ωm)
1	2	1800	0.33	100	200	2000
2	3	1800	0.37	150	300	250
3	5	1800	0.48	175	800	100
Half-space	—	1800	0.49	200	1500	80

Poisson's ratio values derived from joint inversion and previous results (Figure 10d) were in good agreement in the clay layer (the average difference between the two models is equal to 6.2%), but they presented some differences in the dry sand where a maximum difference equal to 31.4% is reached. One would expect a rather low value in this layer (0.25–0.4), and adding some constraints on this parameters should be considered.

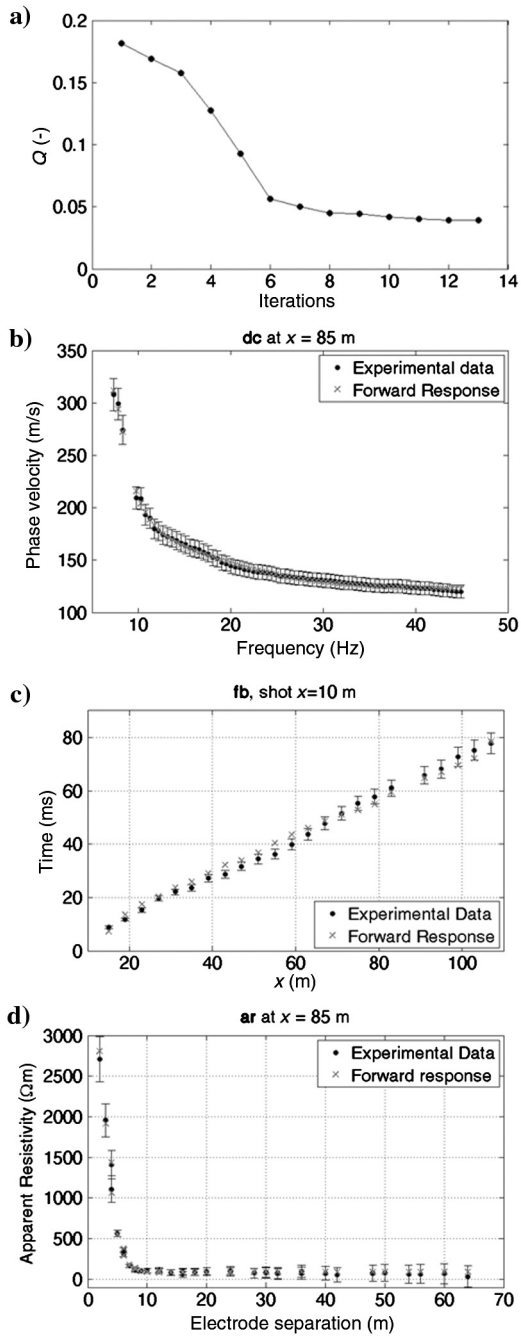

Figure 9. The Hvittingfoss field case: (a) Misfit Q normalized for number of data points at each iteration of the physical joint inversion; examples of misfit between experimental data and forward response of the final model of physical joint inversion are given, for the (b) dispersion curve located at 85 m, (c) P-wave traveltimes of the shot at 10 m, and (d) apparent-resistivity curve located at 85 m.

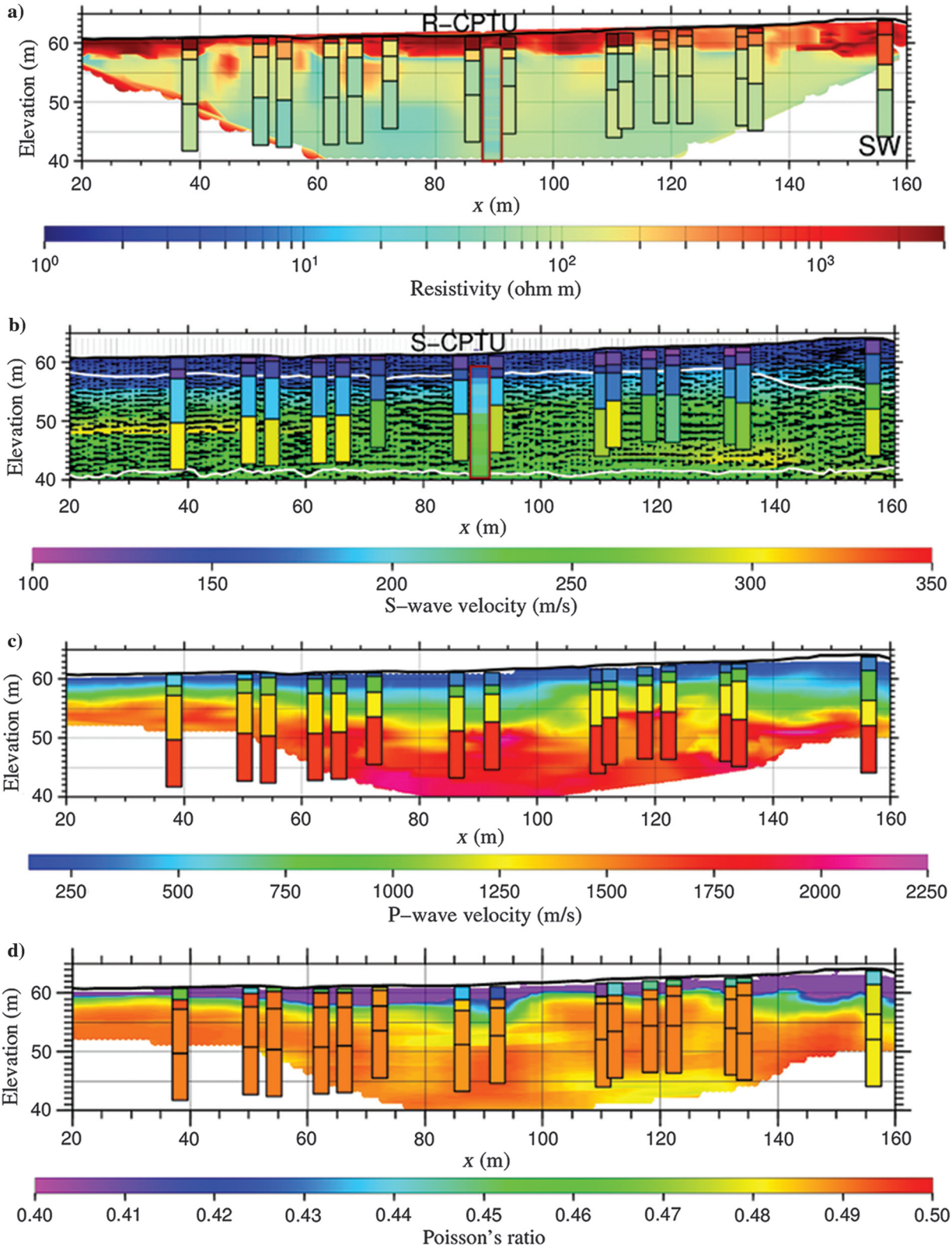

Figure 10. The Hvittingfoss field case: Final 1D models obtained by the physical joint inversion superimposed on previous individual results. In particular, (a) resistivity 1D models and ERT and (b) S-wave velocity 1D models and SH seismic-reflection velocity analysis. The white line corresponds to the interface between the sand and clay layers estimated with GPR. (c) P-wave velocity 1D models with BWT, and (d) Poisson's ratio resulting from the physical joint inversion (bars) superimposed on the distribution computed from the previous results. In panels (a and b), the borehole results (red boxes) are shown with the same color scale.

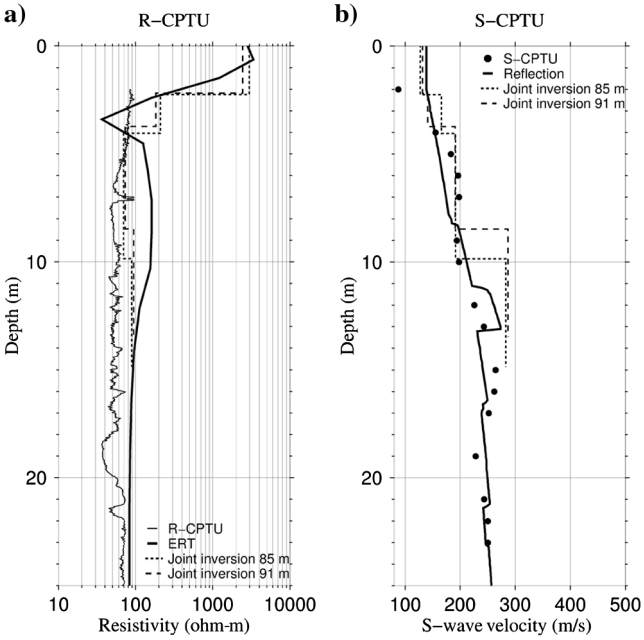

Figure 11. The Hvittingfoss field case: Local comparison at the well location among the joint inversion, borehole, and previous individual results: (a) Resistivity and (b) S-wave velocity.

Figure 11 presents a local comparison between joint inversion, previous individual inversions, and CPTU results at the well location. The joint inversion results fit better the CPTU values than the ones from previous individual inversions. In particular, the resistivity profile extracted from the previous ERT presents an artifact between 2- and 12-m depth with an error greater than 100% with respect to R-CPTU, whereas the joint inversion profiles better estimated the resistivity of the conductive clay layer (Figure 11a). Also, for the S-wave velocity (Figure 11b), the joint inversion provided a better agreement with borehole data.

It is worth mentioning that the investigation depth reached by the joint inversion is lower than the previous studies. This is due to the limitation in the retrieved surface-wave wavelength.

DISCUSSION

We developed the joint inversion approach by adding resistivity data to the algorithm proposed by Boiero and Socco (2014) for seismic surface and P-waves. The same structure was imposed to all the different geophysical parameters, and Poisson's ratio was used as physical link between V_S and V_P. We applied the proposed inversion scheme to a simple synthetic model and compared the results of the joint and individual inversions performed with the same algorithm, the same initial model, and the same constraints on the a priori information. Only the physical joint inversion was applied to a field data set for which previous results from individual 2D smooth inversions were available.

The aim of the analysis of the synthetic data was not to assess the performance of the proposed inversion in complex and realistic parameter distributions but to evaluate the improvement of the joint inversions with respect to the individual inversions. For this reason, we produced a very simple layered model with a gently laterally varying structure. Moreover, the parameterization adopted for the initial model had the same number of layers as the true one. In spite of this, the individual inversions failed in the estimation of some model parameters, which were much better retrieved with the joint inversion approach. The introduction of Poisson's ratio as a physical link between V_S and V_P, although the constrain on this parameter was very weak, further improved the final result (Figure 4). We observed an almost equally good misfit between the synthetic data and the forward response of the final models of the different inversions (i.e., individual, structural, and physical) (Figure 2). This showed that individual inversions could easily fall into a local minimum, whereas the joint inversion approach mitigated the solution nonuniqueness. The layer thickness represented the coupling factor, and a better definition of thicknesses led to an improvement of all the other geophysical parameters (Figure 4). The analysis of the trend of the misfit with iterations (Figure 2d) showed that, with the implemented exit strategy, joint inversion required fewer iterations than individual inversions and provided a lower misfit. Hence, the joint inversion did not imply an increase of computational cost with respect to the individual inversions.

The aim of the field data analysis was to check the performance of the proposed method in a realistic and more complex situation. Moreover, we wanted to compare the performance of our locally 1D layered model assumption with a classical smooth 2D tomographic approach in the case of a laterally varying site.

It is important to remark that the results from previous studies were obtained with significantly different approaches (for details, see Sauvin et al., 2013) from our joint inversion. Previously, P-wave tomography was performed using ReflexW, a commercial code based on finite-difference approximation of the eikonal equation (Sandmeier, 2010); the S-wave model is obtained by computing the interval velocity from the result of the velocity analysis of a high-resolution SH seismic reflection survey; ERT is obtained by Res2DInv, a commercial code based on finite-element 2D forward modeling (Loke, 2010). In our research, we analyzed the same seismic data set for P-wave tomography and the same apparent resistivity data set used for ERT as Sauvin et al. (2013). Our comparison between the previous results and the joint inversion result critically analyzed the performance of the proposed method with respect to well-established approaches routinely used in practice.

Comparison of our result with previous results showed that the lateral variability can be well retrieved despite the assumed parameterization and forward response. The inversion scheme adopted was based on a set of 1D models linked to each other by spatial regularization and hence required the same number of layers for all of the 1D models along the line, without differentiating the parameterization and reference investigation depth in the central portion of the line with respect to the models located at the edges. However, for BWT and ERT, the investigation depth is higher in the central part, whereas for SWA, if the wavelength range is constant along the line, the sensitivity to the deeper layer parameters is constant along the line. In the joint inversion, a compromise between these different investigation depths had to be reached. Hence, the depth extent of the model was lower than the maximum investigation in the central portion, and it was higher at the edges for BWT and CVES. Hence, the V_P and *Rho* of the deeper layers at the edges had very low sensitivity to the data and the values obtained were driven by the regularization and by information coming from SWA.

The survey was performed to reconstruct the geometry and physical properties of the quick clay formation, and so, the main tasks of

the investigation were the identification of the strong resistivity contrast between the dry and high-resistivity sand that overlies the conductive clay layer and the identification of different mechanical properties within the clay layer itself. Comparison between the borehole and ERT results (Figure 11a) highlighted that the presence of the high-resistivity layer on the top of the model produced an artifact in the result of the ERT. Several parameterizations and regularizations were attempted for ERT, leading to similar results (Sauvin et al., 2013). A very low resistivity thin layer was placed underneath the sand, followed by an overestimation of the resistivity in the clay down to approximately a 12-m depth. This artifact was not present in the joint inversion result that was in better agreement with R-CPTU.

Despite that the resistivity estimated with joint inversion was almost constant within the clay unit, the seismic velocities evidence two subunits with different velocities for the P- and S-waves, whereas Poisson's ratio remains constant. This result was in agreement with previous P-wave refraction tomography (Figure 10c) and is possibly related to different consolidations of the clay deposit.

The final model is solved by imposing a constraint on Poisson's ratio that affects the final S- and P-wave velocity values. If this constraint is kept very weak and does not bias the final results but only imposes a physically acceptable value, then the estimation of Poisson's ratio from the final model of the joint inversion is a further product of the inversion, although this parameter is not an unknown of the problem.

Besides the advantages of the joint inversion approach, the field study has confirmed the possibility of using SWA to obtain the S-wave velocity model from the data set that was acquired for P-wave tomography.

Here, we applied a physical link only between the seismic velocities. However, a foreseeable development is the introduction of a petrophysical relationship between seismic velocities and resistivity as shown for the 1D case by Garofalo et al. (2013). This study deals with a physical link between seismic and electric model parameters in a saturated sand layer, and hence that approach is not applicable to this case study.

CONCLUSIONS

We have shown that the joint inversion of surface-wave dispersion curves, P-wave traveltimes, and apparent resistivity provides better results than individual inversions, reducing the nonuniqueness of the solution that leads to interpretation ambiguities. The geometry of the models was well solved, thanks to the contribution of the three different kinds of data, and this also led to an improvement of the estimation of the other geophysical parameters with a reduced number of iterations. The introduction of a physical link through a constraint on Poisson's ratio further improved the results. As a future development, a 2D forward model computation for resistivity should also be considered.

ACKNOWLEDGMENTS

The authors would like to thank P. Podvin for the FDTIMES algorithm to compute the finite-difference solution of the eikonal equation and T. Ingeman-Nielsen for the CR1Dmod algorithm to compute the 1D resistivity effects in electric surveys. We also acknowledge the sponsors of the Ph.D. project of G. Sauvin: the Norwegian Public Roads Administration, the Norwegian National Railway Administration, the Norwegian Water Resources and Energy Directorate, and the International Centre for Geohazards. We are grateful to S. Bazin from the Norwegian Geotechnical Institute for help on the field for the Hvittingfoss data set, P. Bergamo for his comments and suggestions, and M. Asten, K. vanWijk, and two anonymous reviewers for their valuable remarks.

REFERENCES

Aster, R. A., B. Brochers, and C. H. Thurber, 2005, Parameter estimation and inverse problems: Elsevier/Academic Press.

Auken, E., and A. V. Christiansen, 2004, Layered and laterally constrained 2D inversion of resistivity data: Geophysics, **69**, 752–761, doi: 10.1190/1.1759461.

Beaty, K. S., D. R. Schmitt, and M. Sacchi, 2002, Simulated annealing inversion of multimode Rayleigh wave dispersion curves for geological structure: Geophysical Journal International, **151**, 622–631, doi: 10.1046/j.1365-246X.2002.01809.x.

Boiero, D., and L. V. Socco, 2010, Retrieving lateral variations from surface wave dispersion curves: Geophysical Prospecting, **58**, 977–996, doi: 10.1111/j.1365-2478.2010.00877.x.

Boiero, D., and L. V. Socco, 2014, Joint inversion of Rayleigh-wave dispersion and P-wave refraction data for laterally varying models: Geophysics, **79**, no. 4, EN49–EN59, doi: 10.1190/geo2013-0212.1.

Cole, K. S., and R. H. Cole, 1941, Dispersion and absorption in dielectrics, Part I: Alternating current fields: Journal of Chemical Physics, **9**, 341–353, doi: 10.1063/1.1750906.

Comina, C., S. Foti, L. Sambuelli, L. V. Socco, and C. Strobbia, 2002, Joint inversion of VES and surface wave data: Presented at the Symposium on the Application of Geophysics to Engineering and Environmental Problems 2002.

Dal Moro, G., 2008, V_S and V_P vertical profiling via joint inversion of Rayleigh waves and refraction travel times by means of bi-objective evolutionary algorithm: Journal of Applied Geophysics, **66**, 15–24, doi: 10.1016/j.jappgeo.2008.08.002.

Dal Moro, G., M. Pipan, and P. Gabrielli, 2007, Rayleigh wave dispersion curve inversion via genetic algorithms and marginal posterior probability density estimation: Journal of Applied Geophysics, **61**, 39–55, doi: 10.1016/j.jappgeo.2006.04.002.

Dell'Aversana, P., G. Bernasconi, F. Miotti, and D. Rovetta, 2011, Joint inversion of rock properties from sonic, resistivity and density well-log measurements: Geophysical Prospecting, **59**, 1144–1154, doi: 10.1111/j.1365-2478.2011.00996.x.

De Nardis, R., E. Cardarelli, and M. Dobroka, 2005, Quasi-2D hybrid joint inversion of seismic and geoelectric data: Geophysical Prospecting, **53**, 705–716, doi: 10.1111/j.1365-2478.2005.00497.x.

Doetsch, J., N. Linde, and A. Binley, 2010, Structural joint inversion of time-lapse crosshole ERT and GPR traveltime data: Geophysical Research Letters, **37**, L24404, doi: 10.1029/2010GL045482.

Feng, S., T. Sugiyama, and H. Yamanaka, 2005, Effectiveness of multimodel surface wave inversion in shallow engineering site investigation: Exploration Geophysics, **36**, 26–33, doi: 10.1071/EG05026.

Gallardo, L. A., and M. A. Meju, 2003, Characterization of heterogeneous near-surface materials by joint 2D inversion of DC resistivity and seismic data: Geophysical Research Letters, **30**, 1658, doi: 10.1029/2003GL017370.

Gallardo, L. A., and M. A. Meju, 2004, Joint two-dimensional DC resistivity and seismic travel time inversion with cross-gradients constraints: Journal of Geophysical Research, **109**, B03311, doi: 10.1029/2003JB002716.

Gao, G., A. Abubakar, and T. M. Habashy, 2010, Simultaneous joint petrophysical inversion of electromagnetic and seismic measurements: 80th Annual International Meeting, SEG, Expanded Abstracts, 2799–2804.

Gao, G., A. Abubakar, and T. Habashy, 2011, Inversion of porosity and fluid saturations from joint electromagnetic and elastic full-wave form data: 81st Annual International Meeting, SEG, Expanded Abstracts, 660–665.

Garofalo, F., L. V. Socco, and S. Foti, 2013, Joint inversion of surface wave, refracted P-wave and apparent resistivity data to retrieve porosity of saturated layers: 83rd Annual International Meeting, SEG, Expanded Abstracts, 4455–4460.

Haskell, N. A., 1953, The dispersion of surface waves on multilayered media: Bulletin of the Seismological Society of America, **43**, 17–34.

Hering, A., R. Misiek, A. Gyulai, T. Ormos, M. Dobroka, and L. Dresen, 1995, A joint inversion algorithm to process geoelectrical and surface wave seismic data, Part I: Basic ideas: Geophysical Prospecting, **43**, 135–156, doi: 10.1111/j.1365-2478.1995.tb00128.x.

Hu, W., A. Abubakar, and T. M. Habashy, 2009, Joint electromagnetic and seismic inversion using structural constraints: Geophysics, **74**, no. 6, R99–R109, doi: 10.1190/1.3246586.

Jegen, M. D., R. W. Hobbs, P. Tarits, and A. Chave, 2009, Joint inversion of marine magnetotelluric and gravity data incorporating seismic constraints.

Preliminary results of sub-basalt imaging off the Faroe Shelf: Earth and Planetary Science Letters, **282**, 47–55, doi: 10.1016/j.epsl.2009.02.018.
Kis, M., M. Dobròka, and M. Amran, 1995, Joint inversion of geoelectric, refraction and surface-wave seismic data: 57th Annual International Conference and Exhibition, EAGE, Extended Abstracts, P090.
Lai, C. G., 1998, Simultaneous inversion of Rayleigh phase velocity and attenuation for near-surface site characterization: Ph.D. dissertation, Georgia Institute of Technology.
Levenberg, K., 1944, A method for the solution of certain nonlinear problems in least squares: Quarterly of Applied Mathematics, **2**, 164–168.
Linde, N., A. Binley, A. Tryggvason, L. B. Pedersen, and A. Revil, 2006, Improved hydrogeophysical characterization using joint inversion of cross-hole electrical resistance and ground penetrating radar traveltime: Water Resources Research, **42**, W12404, doi: 10.1029/2006WR005131.
Lo, T., and P. I. Inderwiesen, 1994, Fundamentals of seismic tomography: SEG Geophysical Monograph Series 6.
Loke, M. H., 2002, RES2DMOD Version 3.01. Rapid 2D resistivity forward modeling using the finite-difference and finite element methods: Instruction manual.
Loke, M. H., 2010, Res2DInv version 3.59. Geoelectrical imaging 2D and 3D: Instruction manual.
Luke, B., C. Calderòn-Macìas, R. C. Stone, and M. Huynh, 2003, Non-uniqueness in inversion of seismic surface-wave data: Presented at Symposium on the Application of Geophysics to Engineering and Environmental Problems 2003.
Marquardt, D. W., 1963, An algorithm for least squares estimation of nonlinear parameters: Journal of the Society of Industrial Applied Mathematics, **11**, 431–441, doi: 10.1137/0111030.
Meyer, C. D., 2000, Matrix analysis and applied linear algebra: SIAM.
Michalewicz, Z., 2000, Genetic algorithms + data structures = evolution programs: Springer-Verlag.
Misiek, R., A. Liebig, A. Gyulai, T. Ormos, M. Dobroka, and L. Dresen, 1997, A joint inversion algorithm to process geoelectrical and surface wave data, Part II: Application: Geophysical Prospecting, **45**, 65–85, doi: 10.1046/j.1365-2478.1997.3190241.x.
Moorkamp, M., B. Heincke, M. Jegen, A. Roberts, and R. W. Hobbs, 2011, A framework for 3-D joint inversion of MT, gravity and seismic refraction data: Geophysical Journal International, **184**, 477–493, doi: 10.1111/j.1365-246X.2010.04856.x.
Piatti, C., L. V. Socco, D. Boiero, and S. Foti, 2013, Constrained 1D joint inversion of seismic surface waves and P-refraction travel times: Geophysical Prospecting, **61**, 77–93, doi: 10.1111/j.1365-2478.2012.01071.x.
Podvin, P., and I. Lecomte, 1991, Finite difference computation of traveltimes in very contrasted velocity models: A massively parallel approach and its tools: Geophysical Journal International, **105**, 271–284, doi: 10.1111/j.1365-246X.1991.tb03461.x.
Press, F., 1968, Earth models obtained by Monte Carlo inversion: Journal of Geophysical Research, **73**, 5223–5234, doi: 10.1029/JB073i016p05223.
Sandmeier, K. J., 2010, ReflexW version 5.5.1. Windows 9x/NT/2000/XP-program for the processing of seismic, acoustic or electromagnetic reflection, refraction and transmission data. Instruction manual. ReflexW software, www.sandmeier-geo.de, accessed 3 March 2015.
Sauvin, G., I. Lecomte, S. Bazin, J. S. L'Heureux, and M. Vanneste, 2013, Geophysical data integration for quick-clay mapping: The Hvittingfoss case study, Norway, *in* J. S. L'Heureux, A. Locat, S. Leroueil, D. Demers, and J. Locat, eds., Landslides in sensitive clays: From geosciences to risk management: Springer, 229–239.
Socco, L. V., D. Boiero, S. Foti, and R. Wisén, 2009, Laterally constrained inversion of ground roll from seismic reflection records: Geophysics, **74**, no. 6, G35–G45, doi: 10.1190/1.3223636.
Soske, J. L., 1959, The blind zone problem in engineering geophysics: Geophysics, **24**, 359–365, doi: 10.1190/1.1438597.
Tarantola, A., 1987, Inverse problem theory: Methods for data fitting and model parameter estimation: Elsevier Science.
Thomson, W. T., 1950, Transmission of elastic waves through a stratified solid medium: Journal of Applied Physics, **21**, 89–93, doi: 10.1063/1.1699629.
Vozoff, K., and D. L. B. Jupp, 1975, Joint inversion of geophysical data: Geophysical Journal of the Royal Astronomical Society, **42**, 977–991, doi: 10.1111/j.1365-246X.1975.tb06462.x.
Xia, J., R. D. Miller, and C. B. Park, 1999, Estimation of near-surface shear-wave velocity by inversion of Rayleigh waves: Geophysics, **64**, 691–700, doi: 10.1190/1.1444578.